

High-sensitivity and fast-response solar-blind photodetectors via band offset engineering for motion tracking

Received: 3 March 2025

Accepted: 27 August 2025

Published online: 01 September 2025

 Check for updatesHongbin Wang¹, Cheng Zhou¹, Peng Li¹✉, Lin Yang¹, Jiangang Ma¹✉, Ryota Akaike^{2,3}, Hideto Miyake^{2,3}, Haiyang Xu¹✉ & Yichun Liu¹

Single-pixel imaging is emerging as a promising alternative to traditional focal plane array technologies, offering advantages in compactness and cost-effectiveness. However, the lack of solar-blind photodetectors combining fast-response and high-sensitivity has constrained their application in the deep ultraviolet spectrum. This work introduces a self-powered solar-blind photodetector based on a heterostructure comprising a Ga₂O₃ photosensitive layer, an AlN barrier layer, and an N-polar AlGa_N:Si contact layer. The polarization field within the AlN layer induces band bending, creating potential wells that confine photogenerated holes and thereby generate photocurrent gain. Consequently, the Ga₂O₃/AlN/AlGa_N:Si solar-blind photodetector achieves a high responsivity of 0.73 A W⁻¹ and a rapid decay time of 56 μs. This performance enables 256 × 256 resolution solar-blind single-pixel imaging of both static fingerprints and moving objects. The proposed band offset engineering strategy opens a pathway for developing solar-blind photodetectors and solar-blind imaging technologies.

Solar-blind photodetection and imaging systems leverage minimal background interference for diverse military and civilian uses—such as secure communications, missile guidance, flame sensing, corona discharge observation^{1,2}. Current systems predominantly employ silicon-based charge-coupled devices (CCDs), complementary metal-oxide-semiconductor (CMOS) sensors, and photomultiplier tubes (PMTs)^{3–5}. However, CCDs and CMOS sensors necessitate additional filters to block visible and infrared light, increasing system complexity and weight. PMTs, in contrast, are bulky and require high operating voltages. Ultrawide-bandgap semiconductor focal plane arrays offer a compact alternative for solar-blind imaging, but face challenges related to complex integration process^{6–8}. Recently, several groups have recently reported solar-blind imaging using single ultrawide-bandgap semiconductor photodetector with two-dimensional scanning^{9–11}. Nevertheless, the pixel-by-pixel scanning process remains too slow for real-time imaging. In contrast, the single-pixel imaging technique

leverages structured light modulation to capture spatial scene details, utilizing only one photodetector to record the modulated light intensity (Fig. 1a). This approach offers the benefits of rapid image capture and has recently been demonstrated in the visible and X-ray spectra^{12–14}, positioning it as a promising technology for solar-blind imaging applications.

Achieving photodetectors with high sensitivity (>0.1 A W⁻¹) and fast response speed (<1 ms) is essential for solar-blind single-pixel imaging. While ultra-wide bandgap semiconductors are effective as solar-blind photosensitive materials, the challenge of bipolar doping in ultra-wide bandgap semiconductors restricts solar-blind photodetectors to photoconductive and heterojunction-based configurations^{15,16}. Photoconductive devices rely on defect-related minority carrier trapping to achieve high responsivity, but suffer from prolonged response times due to extended minority carrier lifetimes. In contrast, photovoltaic devices utilize the built-in electric fields at

¹State Key Laboratory of Integrated Optoelectronics, Key Laboratory for UV Light-Emitting Materials and Technology of Ministry of Education, School of Physics, Northeast Normal University, Changchun, China. ²Graduate School of Engineering, Mie University, Tsu, Mie, Japan. ³Innovation Center for Semiconductor and Digital Future, Mie University, Tsu, Mie, Japan. ✉ e-mail: lip032@nenu.edu.cn; majg@nenu.edu.cn; hyxu@nenu.edu.cn

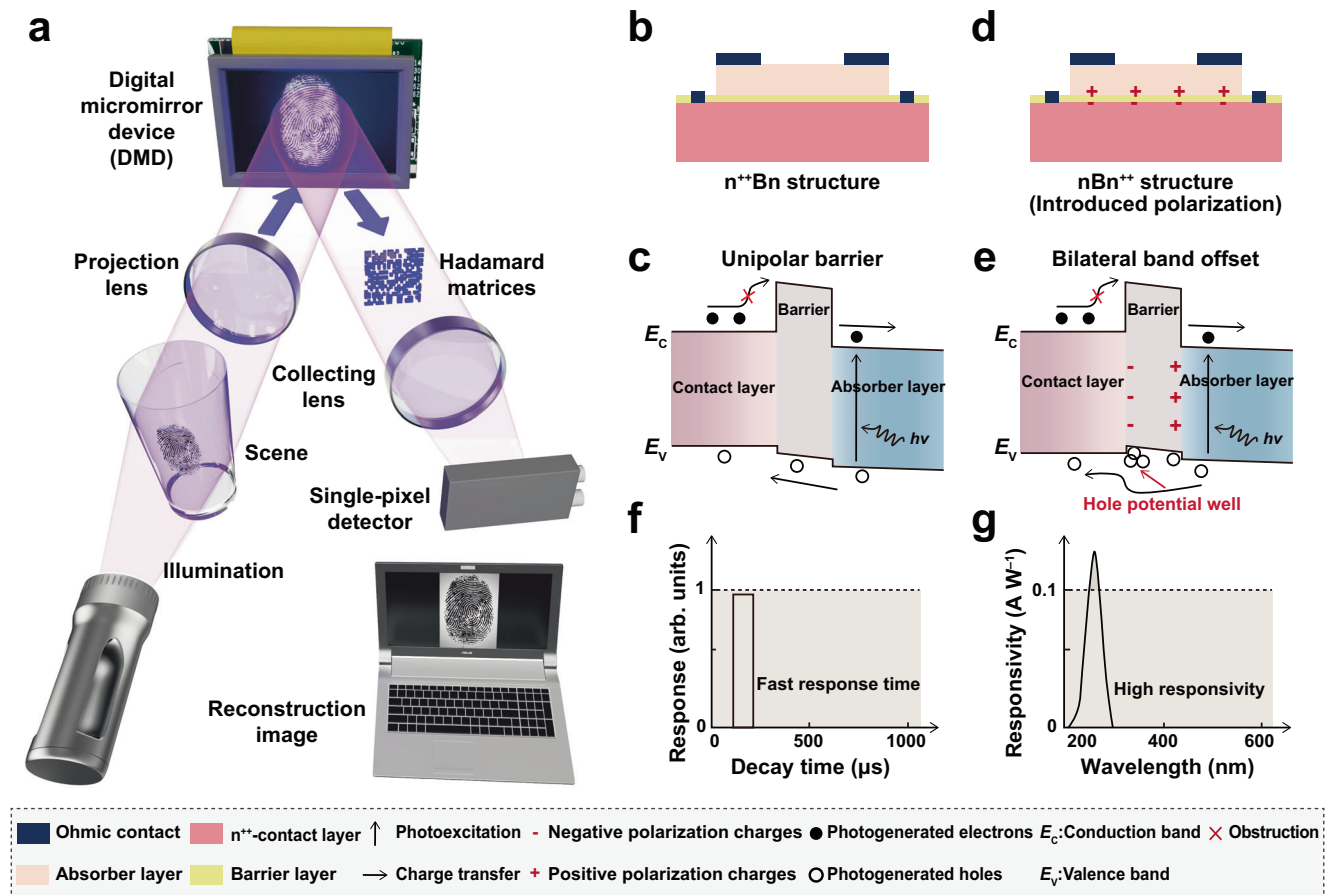


Fig. 1 | Designed solar-blind imaging system and required solar-blind photodetectors. **a** Illustration of a single-pixel imaging system, detailing its primary components including the light source, target object, digital micromirror device, and a detector. The diagrams illustrate the device structure (**b**) and carrier dynamic process (**c**) in nBn^{++} junctions without polarization charges at the interfaces. The

diagrams illustrate the device structure (**d**) and carrier dynamic processes (**e**) in nBn^{++} junctions with polarization charges at the interfaces. Fast response speed (**f**) and high responsivity (**g**) of a solar-blind photodetector that are required for single-pixel imaging application.

heterojunctions and Schottky junctions to regulate carrier dynamics, eliminating the need for external bias and thereby simplifying the detection systems. However, band discontinuities and limited Fermi-level differences in semiconductor heterojunctions impede efficient separation of photogenerated carriers, resulting in reduced responsivity and poor spectral selectivity (Supplementary Figs. 1, 2).

To address the aforementioned challenges, various solutions have been proposed. One approach is to utilize photodetectors based on the unipolar barrier n -photosensitive layer/barrier/ n^{++} -contact (nBn^{++}) structure (Fig. 1b). This architecture features a conduction band offset that blocks electron transport, reducing dark current without suppressing the photocurrent^{17–19}. Concurrently, the valence band remains nearly continuous, facilitating unimpeded flow of holes (Fig. 1c). Additionally, integrating polarization effects into an nBn^{++} junction (Fig. 1d) enables modulation of band bending at the interface. Certain compound semiconductors (e.g., GaN, ZnO) exhibit spontaneous polarization due to the inherent inversion asymmetry in their wurtzite crystal structure^{20–22}, with polarization orientation determined by the stacking of cations and anions^{23,24}. Through appropriate design, a potential well of holes can be engineered at the nBn^{++} interface, which promotes the accumulation of photogenerated holes within the barrier layer (Fig. 1e). This triggers a gain mechanism that enhances the device's responsivity. Nevertheless, the built-in electric field extracts the accumulated photogenerated holes, ensuring a rapid response time. This bilateral band offset strategy enhances external quantum efficiency (EQE) without compromising the response speed,

opening a avenue for high-performance optoelectronic devices (Fig. 1f, g).

In this work, we fabricate a self-powered solar-blind photodetector based on a $Ga_2O_3/AlN/AlGaN:Si$ (nBn^{++}) heterojunction, where Ga_2O_3 serves as the absorber, AlN as the barrier, and AlGaN:Si as the contact layer. The intrinsic differences in energy band structure and orbital compositions between Ga_2O_3 and III-nitrides enable the formation of an nBn^{++} junction. Experimental characterization and theoretical simulations confirm the establishment of a bilateral band offset in the $Ga_2O_3/AlN/N$ -polar AlGaN:Si heterojunction, incorporating the spontaneous polarization effect of N-polar nitrides. The AlN/AlGaN:Si layers generate a polarization field at the interface, creating a potential well for photogenerated holes that enables high responsivity and rapid response speed. Leveraging this high-performance photodetector, we demonstrate solar-blind imaging of both fingerprints and moving objects, underscoring its potential for imaging applications.

Results

Surface polarity and heteroepitaxial relationships

The microstructural characteristics of the multilayer heterostructure films were elucidated using spherical aberration-corrected transmission electron microscopy (AC-TEM), high-resolution X-ray diffraction (XRD), and atomic force microscopy (AFM). Figure 2a and Supplementary Fig. 3 present the cross-sectional morphology and corresponding elemental mappings of the Ga_2O_3/AlN (II)/AlGaN:Si/AlN (I) stack on a c -plane sapphire substrate, with each layer exhibiting

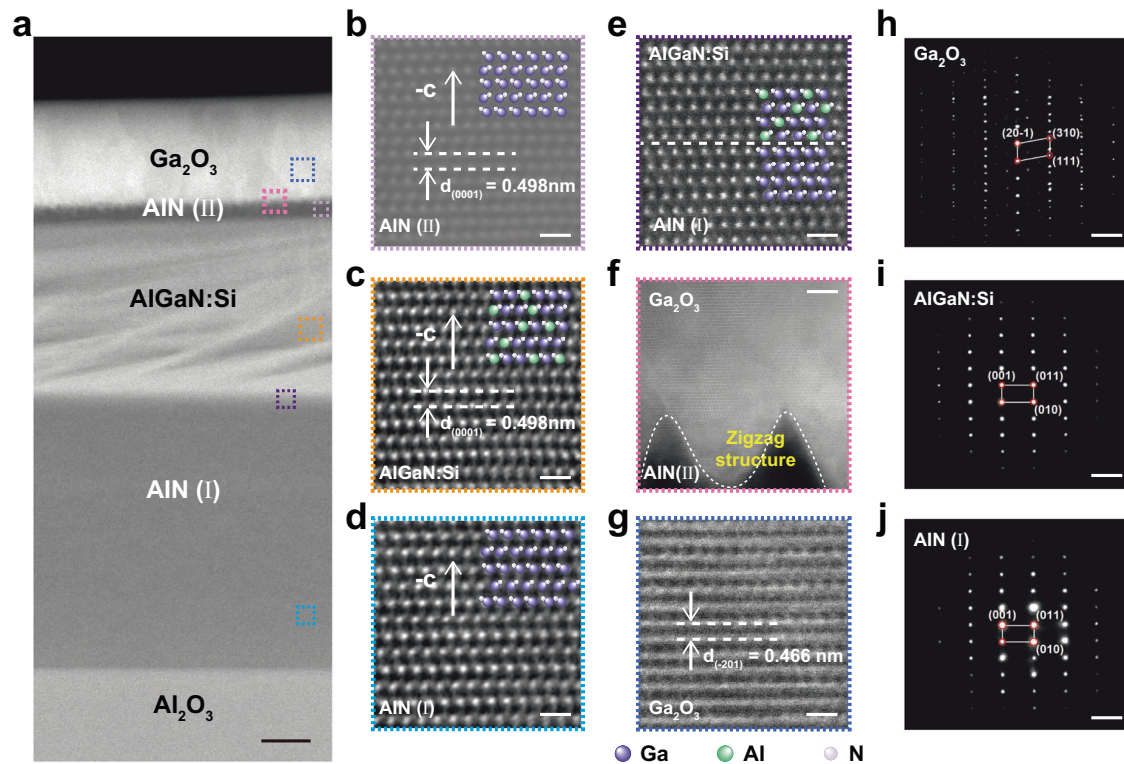


Fig. 2 | Atomic structure of epitaxially grown Ga_2O_3 on N-polar nitrides. **a** AC-TEM image of the $\text{Ga}_2\text{O}_3/\text{AlN}(\text{II})/\text{AlGaN:Si}/\text{AlN}(\text{I})$ stack on a c-plane sapphire substrate. Scale bar, 200 nm. High-magnification AC-TEM images of the upper AlN (II) layer (**b**), AlGaN:Si layer (**c**) and bottom AlN (I) layer (**d**), respectively. Atomic arrangement diagrams inserted in highlight the N-polarity of the nitrides. The dashed white lines indicate the interplanar spacings corresponding to (001) of AlN.

e High-magnification AC-TEM image of the AlGaN:Si/AlN (I) interface area, illustrating that the AlGaN:Si layer maintains the N-polarity of the AlN (I) template. Scale bar, 1 nm. High-magnification AC-TEM image of the $\text{Ga}_2\text{O}_3/\text{AlN}(\text{II})$ interface area (**f**) and Ga_2O_3 layer (**g**), showing a zigzag structure in AlN (II)-assisted nucleation growth model in Ga_2O_3 . Scale bars, 5 nm (**f**); 1 nm (**g**). FFT patterns of the Ga_2O_3 (**h**), AlGaN:Si (**i**), and AlN (I) layers (**j**). Scale bars, 5 nm^{-1} .

distinct contrast and well-defined interfacial boundaries. The thicknesses of the Ga_2O_3 , AlN (II), AlGaN:Si, and AlN (I) films are approximately 250, 30, 300, and 700 nm, respectively. The crystalline quality of each layer was assessed based on high-resolution TEM (HRTEM) images and the full width at half-maximum values of XRD rocking curves. As depicted in Fig. 2b–d, the HRTEM images reveal highly ordered Al/Ga and N atomic arrangements within the AlN (II), AlGaN:Si, and AlN (I) layers. These images confirm that both AlN (II) and AlGaN:Si exhibit N-polarity, inheriting the polarity from the underlying AlN (I) template (Fig. 2e) prepared via a high-temperature annealing technique^{25,26}. The Al and Ga contents in the AlGaN:Si film are determined to be 0.7 and 0.3, respectively, based on XRD 2θ - ω scan measurements. The screw and edge dislocation densities in the AlGaN:Si layer are determined to be less than $3 \times 10^8 \text{ cm}^{-2}$ and $8 \times 10^8 \text{ cm}^{-2}$, respectively (Supplementary Fig. 4b). These low dislocation densities are comparable to those reported for high-quality Al-polar AlGaN^{27–29}. The superior crystalline quality of the N-polar nitrides can be attributed to the high growth temperature and the large offset angle of the substrate, which suppress complex island nucleation and coarsening, facilitate the migration of Al atoms, and lead to a step-flow growth mode with reduced dislocation densities. This is consistent with the steps and terraces observed at the AlN (II)/AlGaN:Si interface in the TEM and the AFM (Supplementary Fig. 4c) images.

Figure 2f, g display HRTEM images obtained at the $\text{Ga}_2\text{O}_3/\text{AlN}(\text{II})$ interface and within the Ga_2O_3 layer, respectively. The AlN (II) surface exhibits a zigzag structure, as indicated by the white dashed lines, which is considered advantageous for the nucleation and growth of Ga_2O_3 and the subsequent dislocation annihilation as the film thickness increases. The Ga_2O_3 film grown on AlN (II) manifests a β -phase polycrystalline structure with (-201) orientation (Supplementary

Fig. 4a). The high-quality growth of Ga_2O_3 is attributed to its minimal lattice mismatch with AlN. Supplementary Fig. 5 illustrates the similar hexagonal ordering of Ga/O atoms in Ga_2O_3 and Al/N atoms in AlN. Despite this structural similarity, their atomic spacings differ: O atoms spacing on the Ga_2O_3 (-201) plane are 2.853 Å and 3.04 Å, while N atoms spacing on the AlN (001) plane is 3.11 Å. The differences correspond to lattice mismatches of 2.6% and 6.2% between these two planes. The above crystallographic structure analyses figure out an epitaxial relationship of $[-201] \beta\text{-Ga}_2\text{O}_3/[001] \text{AlN}/[001] \text{AlGaN:Si}$. The epitaxial structure was further elucidated through Fast Fourier Transform (FFT) analysis. For Ga_2O_3 , the diffraction spots manifest a well-ordered lattice structure (Fig. 2h). The measured lattice plane spacings of 0.466 nm, 0.249 nm, and 0.235 nm are identified as the $(20-1)$, (111) , and (310) planes, respectively. FFT patterns for AlGaN:Si and AlN (I) exhibit consistent arrangements (Fig. 2i, j), confirming an epitaxial relationship along the $[001]$ crystallographic direction.

Photoresponse characteristics of solar-blind photodetectors

Figure 3a presents the structural schematic of the solar-blind photodetector fabricated through standard photolithography, dry etching, and lift-off processes (Supplementary Fig. 6). This heterojunction device, featuring thickness-optimized AlN layers (Supplementary Fig. 7), was engineered to evaluate the photoresponse of the $\text{Ga}_2\text{O}_3/\text{AlN}/\text{AlGaN:Si}$ heterojunction under 245 nm deep-ultraviolet light illumination. Figure 3b illustrates the semi-logarithmic current-voltage (I - V) curves in both dark and illuminated states at varying light intensities. The observed nonlinear I - V characteristics with a rectification ratio exceeding 10^2 within $\pm 2 \text{ V}$, considering the measured quasi-Ohmic contacts between metal electrodes and Ga_2O_3 or AlGaN:Si (Supplementary Fig. 8a). The abrupt increase in dark current beyond

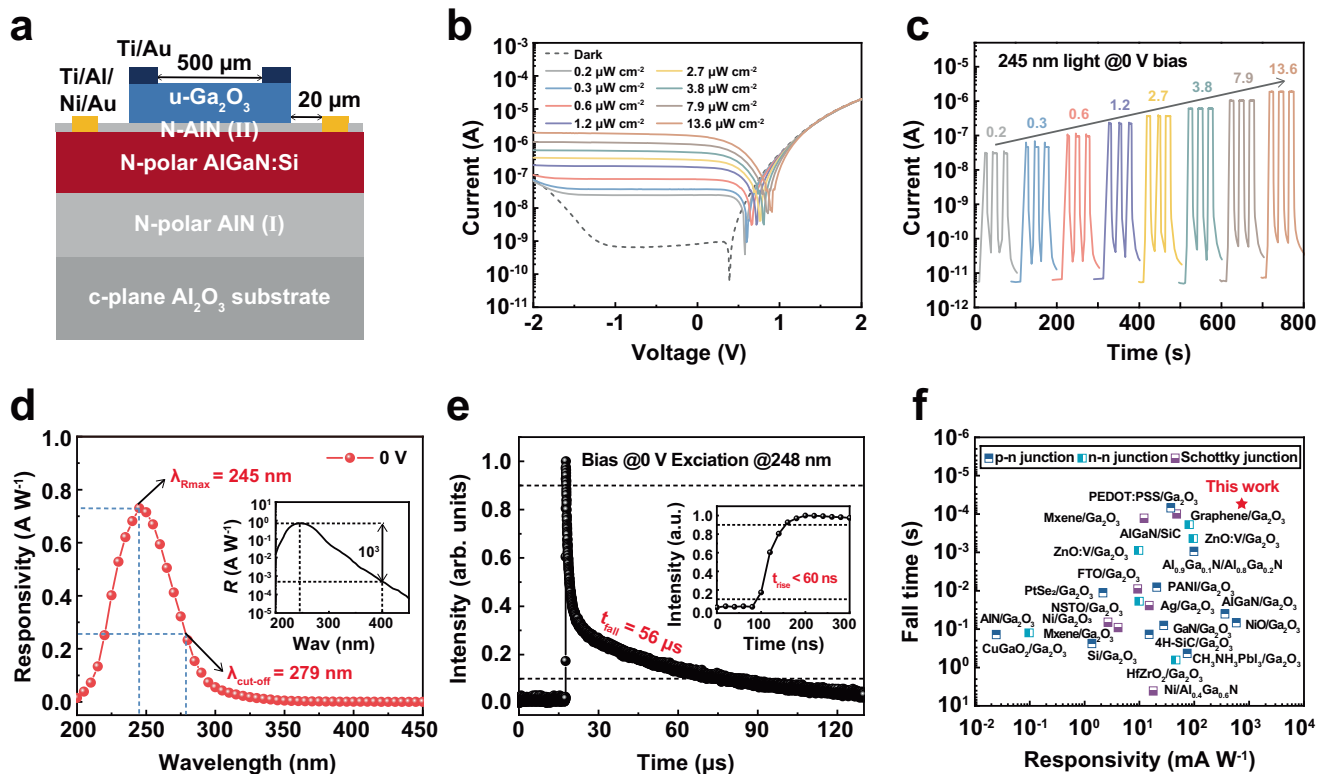


Fig. 3 | Self-powered solar-blind photodetection performance. **a** Schematic illustration of the Ga₂O₃/AlN/AlGaN:Si photodetector. Semi-logarithmic plots of the current-voltage (**b**) and current-time characteristics (**c**) in the dark and under illumination with varying intensities of 245 nm light. **d** Wavelength-dependent responsivity of the device at 0 V, with the semi-logarithmic representation

provided in the inset. **e** Transient photoresponse characteristic curve obtained using a 248 nm pulsed laser at 0 V. The inset shows the response rise time curve. **f** Comparison of responsivity and fall time of the Ga₂O₃/AlN/AlGaN:Si photodetector with those of Ga₂O₃ and AlGaN p-n, n-n, and Schottky junction solar-blind photodetectors.

-1 V is attributed to electric field-assisted tunneling^{30–32}. The current-time (*I*-*t*) curves in Fig. 3c demonstrate that the device can switch between on and off states with high reproducibility under varying light intensities. The photocurrent (*I*_{ph}) of 24.8 nA is achieved at 0 V when the device is irradiated by 0.2 μW cm⁻² light, and it increases to 1.9 μA at a higher light power density (*P*) of 13.6 μW cm⁻². By fitting the photocurrent versus light power curve, a value *θ* of 0.92 is obtained (Supplementary Fig. 8b), indicating a near-linear correlation between them. This suggests that the device possesses a small number of deep-level traps and interface states, which in turn diminishes the probability of carrier recombination during photoexcitation and charge transport processes^{33,34}.

To comprehensively evaluate the photodetection capabilities of the device, its critical parameters were analyzed. The calculated photo-to-dark current ratio (PDCR) at 0 V demonstrates a near-linear progression with the increase of light intensity, reaching a peak of 3.5 × 10⁵ at 13.6 μW cm⁻² and sustaining above 10³ even under a low light intensity of 0.2 μW cm⁻² (Supplementary Fig. 8c), underscoring the device's ability to detect weak optical signals. The responsivity shows a trend of decrease with the increase of light intensity (Supplementary Fig. 8d), and a peak responsivity of 0.73 A W⁻¹ was obtained at 245 nm and a rejection ratio (*R*_{245 nm}/*R*_{400 nm}) of 2 × 10³ (Fig. 3d), confirming the device's selective response to solar-blind signals. The zero-bias detectivity achieves a maximum value of 2.9 × 10¹¹ Jones owing to low

noise equivalent power of 1.5 × 10⁻¹³ W Hz^{-1/2} (Supplementary Fig. 8e), indicating a high signal-to-noise ratio. High responsivity and detectivity imply the presence of internal gain mechanisms even at 0 V. This concurs with the observed EQE of 369% (Supplementary Fig. 8f). Furthermore, the rise and fall times, defined as the interval between 10 and 90% of the maximum photoresponse values, are 60 ns and 56 μs, respectively (Fig. 3e). The difference between rise and fall times arises from the asymmetric carrier transport mechanisms governed by the polarization field and valence potential well. Upon illumination, photogenerated carriers are generated on a picosecond timescale, and the strong polarization field accelerates the separation and collection of photogenerated carriers, resulting in a short rise time. Conversely, when illumination is terminated, the fall time is dominated by the hole de-trapping process at valence potential well, thereby leading to a long fall time. We also measured the RC time constant using a square wave signal generator and an oscilloscope. The measured RC time constant value of 3.0 μs confirms that the RC time constant does not serve as a limiting factor for the device's response time. Furthermore, we have conducted multiple pulses measurements and evaluated the intensity-dependent response time (Supplementary Fig. 9). The device demonstrates stability under multiple pulses of different light intensities. The fall times shorten slightly with increasing light intensity, which may be caused by the enhancement of carrier drift and potential well saturation effect^{35,36}. Taking advantage of the fast response speed of Ga₂O₃/AlN/AlGaN:Si photodetector, a self-powered optical communication system was demonstrated, capable of transmitting the signals at a 800 bit s⁻¹ transmission rate (Supplementary Fig. 10).

To highlight the performance of the Ga₂O₃/AlN/AlGaN:Si photodetector, a thorough comparative analysis of its responsivity, photo-to-dark current ratio, detectivity, EQE, and rise/fall times was

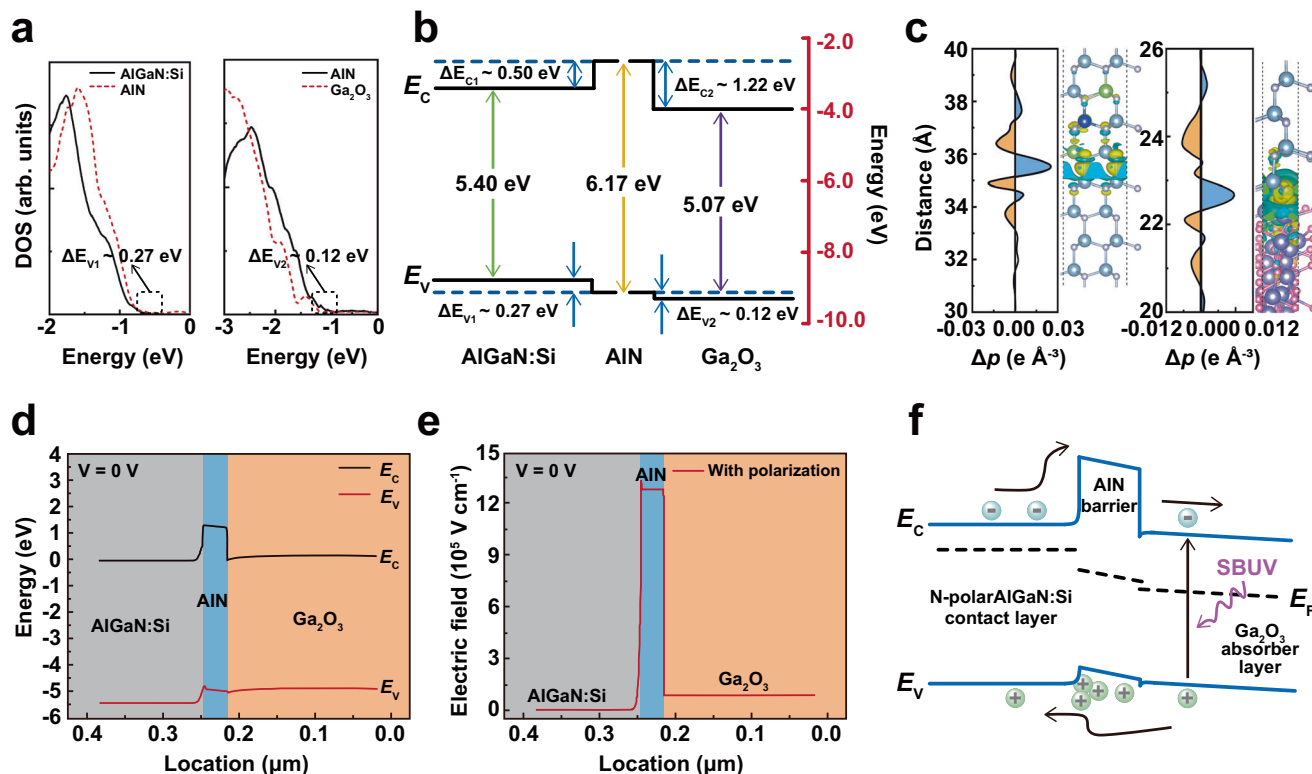


Fig. 4 | Energy band diagram and electric field profile of the Ga₂O₃/AlN/AlGaIn:Si heterojunction. **a** Density of states (DOS) for AlGaIn:Si and AlN, and AlN and Ga₂O₃. **b** Band alignment of AlGaIn:Si/AlN and AlN/Ga₂O₃ interfaces in the absence of polarization effects. **c** Charge displacement and charge differences

curves of the AlGaIn:Si/AlN and AlN/Ga₂O₃ interfaces. Energy band diagram (**d**) and electric field profile (**e**) across the Ga₂O₃/AlN/AlGaIn:Si heterojunction under the polarization. **f** Energy band diagram illustrating the photodetection mechanism of the Ga₂O₃/AlN/AlGaIn:Si heterojunction.

conducted against Ga₂O₃ and AlGaN self-powered solar-blind photodetectors reported so far. As depicted in Fig. 3f and detailed in Supplementary Table 1, our Ga₂O₃/AlN/AlGaIn:Si photodetector demonstrates higher signal-to-noise ratio and improved spectral selectivity. Particularly, high responsivity and rapid response speed were achieved simultaneously, which is challenging for the conventional p-n, n-n heterojunction and Schottky junction solar-blind photodetectors. To assess device reliability and reproducibility, we conducted systematic characterization of photoresponse parameters (including responsivity and fall time) across 10 independently fabricated devices (Supplementary Fig. 11). Statistical analysis reveals that 90% of the devices demonstrate responsivity values above 0.6 A W⁻¹, while 70% achieve fall times shorter than 60 μs, confirming consistency in device performance. In addition, we also conducted continuous illumination stability test (Supplementary Fig. 12). The photocurrent remains at 10⁻⁶ A for 90% of the total illumination time (10³–10⁴ s) with no measurable decay. The results indicate that the photodetector has long-term operation reliability and stability. These characteristics of Ga₂O₃/AlN/AlGaIn:Si photodetectors demonstrate potential for applications in high-resolution solar-blind imaging systems.

Modulation of carrier dynamics by bilateral band offsets

To elucidate the mechanism behind the high photodetection performance, we investigated the energy band alignment that governs the carrier transport and recombination processes in the Ga₂O₃/AlN/AlGaIn:Si heterojunction through a combination of experimental characterization and theoretical simulations. To characterize the band alignment of the Ga₂O₃/AlN/AlGaIn:Si heterostructure, we first performed X-ray photoelectron spectroscopy (XPS) (Supplementary Fig. 13a–c). Using Kraut's method, valence band offsets (ΔE_v) were determined from binding energy differences between the valence

band maximum (VBM) and core-level shifts. The resulting ΔE_v values were 0.09 eV for Ga₂O₃/AlN and 0.28 eV for AlN/AlGaIn:Si. Then, using the bandgap values of Ga₂O₃ (5.02 eV, Supplementary Fig. 13d), AlGaIn:Si (5.39 eV, Supplementary Fig. 13e), and AlN (6.2 eV)^{37–39}, we calculated conduction-band offsets (ΔE_c) of 1.27 eV for Ga₂O₃/AlN and 0.53 eV for AlN/AlGaIn:Si. Consequently, the equilibrium band diagram for Ga₂O₃/AlN/AlGaIn:Si heterostructure (Supplementary Fig. 13f), without considering polarization effects, exhibits unipolar barrier characteristics, which can suppress electron leakage from AlGaIn:Si to Ga₂O₃ while allowing hole transport from Ga₂O₃ to AlGaIn:Si.

To probe the engineered band structure, we performed density functional theory (DFT) simulations. Figure 4a presents the valence band density of states (DOS) at the AlGaIn:Si/AlN and AlN/Ga₂O₃ interfaces. The valence band offsets (ΔE_v) for the AlGaIn:Si/AlN and AlN/Ga₂O₃ heterojunctions are 0.27 and 0.12 eV. The bandgaps of Ga₂O₃, AlN, and AlGaIn:Si were calculated using the HSE06 hybrid functional, resulting in values of 5.07, 6.17, and 5.40 eV, respectively (Supplementary Fig. 14), which are in agreement with the results obtained by the Tauc-plot method based on ultraviolet-visible absorption spectroscopy. The conduction band offsets (ΔE_c) for the AlGaIn:Si/AlN and AlN/Ga₂O₃ heterojunctions are 0.50 and 1.22 eV, respectively. Experimental results are confirmed by the simulated band diagram in Fig. 4b, which exhibits a conduction band electron-blocking barrier. The differential charge density in Fig. 4c reveals electron accumulation (yellow contours) at both AlGaIn:Si/AlN and AlN/Ga₂O₃ junctions. This signifies electron sharing and hybridization between bonded Al-N and Ga-N atoms.

Based on the relative energy levels and bandgaps of Ga₂O₃, AlN, and AlGaIn:Si, we further simulated the energy band alignment of the heterojunction using technology computer aided design (TCAD), taking into account the effects of polarization (Fig. 4d). The observed

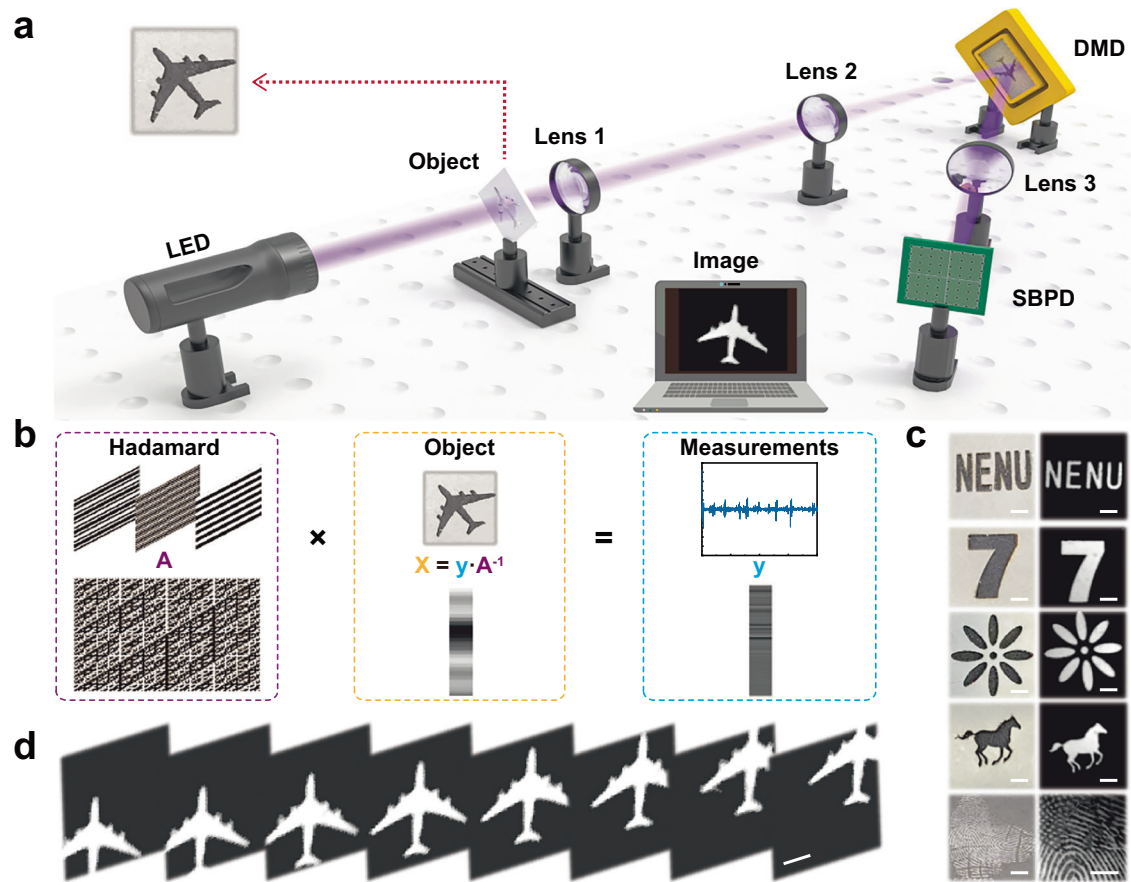


Fig. 5 | Solar-blind ultraviolet imaging of moving and stationary objects. **a** Illustration of the experimental setup for single-pixel imaging. **b** Principle of single-pixel imaging, utilizing the Hadamard matrix for light field modulation. **c** Imaged samples (left) including the letter “NENU”, the number “7”, and patterns of

“flower”, “horse”, and “fingerprint”, along with their corresponding reconstructed 256 × 256-pixel images (right). Scale bars, 3 mm. **d** Real-time imaging of a moving “airplane” with a resolution of 64 × 64 pixels. Scale bars, 3 mm.

downward and upward shifts in the energy bands of AlGaIn:Si and AlN can be attributed to the negative polarization charges at the N-polar AlGaIn:Si/AlN interface, which result in a valence band hole potential well. Figure 4e illustrates the simulated electric field strength of the Ga₂O₃/AlN/AlGaIn:Si heterojunction. The electric field intensity within the Ga₂O₃ layer reaches 8×10^4 V cm⁻¹, close to the built-in potential (2.28 V) calculated from the capacitance-voltage (C–V) curve (Supplementary Fig. 15), which is higher than that reported for Ga₂O₃-based Schottky junction and heterojunction devices (Supplemental Table 2). C–V measurements reveal a depletion width of 534 nm, exceeding the Ga₂O₃ layer’s intrinsic thickness (250 nm). This confirms complete layer depletion, inducing uniform band bending throughout Ga₂O₃ that enhances photogenerated carrier separation. The resulting photodetection mechanism in the Ga₂O₃/AlN/AlGaIn:Si heterojunction (Fig. 4f) operates as follows. Under solar-blind ultraviolet illumination, photogenerated electron-hole pairs primarily form in the Ga₂O₃ layer. The built-in electric field separates these carriers, with electrons rapidly extracted by the top electrode while holes drift toward the AlN layer. These holes accumulate in the valence band potential well at the AlGaIn:Si/AlN interface, extending their lifetime. To maintain charge neutrality, electrons are subsequently injected into the depletion region. Given electrons’ higher mobility ($\mu_e > \mu_h$), they undergo multiple transits during a hole’s lifetime, generating photocurrent gain. This polarization-engineered gain mechanism is evidenced by 200–1000% EQE values reported in similar photodetectors^{40–45}. Upon illumination termination, the strong polarization field within AlN rapidly extracts trapped holes, accelerating the response fall time.

High-resolution solar-blind single-pixel imaging

We incorporated the high-performance Ga₂O₃/AlN/AlGaIn:Si photodetector into a single-pixel imaging system to highlight its potential for practical applications. As illustrated in Fig. 5a, b, the imaging setup and principle involve solar-blind ultraviolet light illuminating the target object, which is then projected onto a digital micromirror device (DMD) through a lens. The spatially modulated light pattern from the DMD is optically coupled to the photodetector. Computational reconstruction of the object image is achieved by decoding the detected intensity signals against the corresponding DMD modulation patterns. The Hadamard matrix, denoted by the letter A within the purple dotted line box, functions as the light field modulation for the single-pixel imaging process. The object is reconstituted as a one-dimensional column vector, indicated by the letter X within the yellow dotted line box. The interaction between the object and the matrix composed of all rows of the Hadamard matrix produces a one-dimensional vector, represented by the letter y within the blue dotted line box, which is captured by the photodetector. Subsequently, the object information X is extracted using an inverse method ($X = y \cdot A^{-1}$), thereby enabling the reconstruction of the object image (see Supplementary Note 1 for details).

Figure 5c displays a range of typical objects, including letters, numbers, patterns, and fingerprints, along with their corresponding solar-blind ultraviolet images, with a resolution of 256 × 256 pixels. The high-resolution imaging capability of the system is demonstrated by the clear overlapping fingerprint images. Real-time imaging is achieved with a stepper motor-driven target positioning system. As shown in

Fig. 5d, the detection module keeps counting as the object moves from the bottom-left to the top-right corner. To enable dynamic visualization of moving objects, a sequence of 150 consecutively acquired images (64×64 pixels) was processed into an 8s video and included as Supplementary movie 1. The video effectively conveys details such as the wings and propellers of the moving airplane. In addition, the device distinctly captures alphanumeric characters in motion (Supplementary movie 2). These results confirm that the system achieves real-time dynamic tracking capabilities. This work represents the demonstration of dynamic imaging in the solar-blind spectral region using a single device—a capability unattainable with array detectors (see Supplementary Note 2 for details).

Discussion

In summary, we have demonstrated a self-powered solar-blind photodetector based on a polarization-engineered $\text{Ga}_2\text{O}_3/\text{AlN}/\text{AlGaN}:\text{Si}$ heterojunction that overcomes the inherent trade-off between responsivity and response speed in solar-blind imaging. By harnessing the polarization field in the N-polar $\text{AlN}/\text{AlGaN}:\text{Si}$ barrier structure, we induced tailored band bending to create hole-confining potential wells—enabling high responsivity (0.73 A W^{-1}) and rapid carrier extraction ($56 \mu\text{s}$ decay time) without external bias. This bilateral band offset design resolves long-standing limitations of heterojunction-based photodetectors by simultaneously enhancing photogenerated carrier confinement and transport. Crucially, this device achieves 256×256 resolution single-pixel imaging of both static fingerprints and dynamic moving targets under solar-blind illumination, underscoring its viability for real-time applications. Our work establishes a polarization-driven band engineering strategy as a pathway toward next-generation optoelectronic devices, unlocking frontiers in high-performance solar-blind sensing and computational imaging.

Methods

Film growth

The fabrication of the $\text{Ga}_2\text{O}_3/\text{AlN}/\text{AlGaN}:\text{Si}$ heterostructure started from the development of face-to-face annealed sputter-deposited AlN (FFA Sp-AlN) substrates. Specifically, a 99.9999% pure AlN target was utilized for magnetron sputtering, with a c-plane sapphire substrate that was offset by 5.0° from the m -axis to create 300 nm thick N-polar FFA Sp-AlN substrates characterized by reduced threading dislocation densities. Subsequent to this, metal-organic chemical vapor deposition (MOCVD) was employed to grow AlN and AlGaN:Si layers on the N-polar FFA Sp-AlN substrates. Initially, a 300 nm MOCVD AlN layer was grown to obtain a smooth template surface at a temperature of 1400°C , a V/III molar ratio of 161, a chamber pressure of 30 Torr, and using trimethylaluminum (TMAI) and ammonia (NH_3) as the source materials, with hydrogen as the carrier gas. Following this, the AlGaN:Si n-type contact layer was deposited on the N-polar AlN (I) substrates using trimethylgallium (TMGa), TMAI, NH_3 , and silane (SiH_4) as source materials. The AlGaN:Si layer was grown at 1250°C and a pressure of 60 Torr, with a SiH_4 flow rate of 10 nmol/min. The high growth temperature was critical to prevent the formation of hillock structures in N-polar AlGaN:Si films grown at the lower temperature of 1150°C , which occurs due to the inadequate diffusion length of Al atoms that fail to span the terrace width. The N-polar AlGaN:Si was obtained by face-to-face annealing sputtering deposition of N-polar AlN as the template, with a 5.0° off-cut angle substrate and a growth temperature of 1250°C . The carrier concentration of N-polar AlGaN:Si was measured to be $1.46 \times 10^{18} \text{ cm}^{-3}$ with a mobility value of $32.9 \text{ cm}^2 \text{ V}^{-1} \text{ s}^{-1}$ by Hall measurement at room temperature. Subsequently, an AlN (II) buffer layer was deposited atop the AlGaN:Si surface utilizing a nitride/oxide double cavity MOCVD system. Prior to the growth process, the sample was subjected to hydrogen treatment at 1050°C to eliminate surface impurities. The AlN (II) layer was then grown at a temperature of 1150°C . To complete the structure, an unintentionally

doped Ga_2O_3 layer was epitaxially grown on the AlN (II) buffer layer at 900°C , using TEGa as the precursor, oxygen as the reactive gas, and Ar as the carrier gas.

Device fabrication

The as-grown samples underwent a sequential cleaning process with acetone, isopropanol, and de-ionized water prior to device fabrication. To access the N-polar AlGaN:Si n-type contact layer, toroidal isolation patterns were created on a photoresist mask using photolithography. Subsequently, the Ga_2O_3 and AlN layers were etched to depths of about 250 nm and 50 nm through two-step photolithography and chlorine-based inductively coupled plasma (ICP) dry etching technique. Following this, toroidal Ti/Al/Ni/Au (20/100/40/50 nm) electrodes and Ti/Au (20/50 nm) metal stacks were deposited on the AlGaN:Si and Ga_2O_3 surfaces, respectively, through a combination of photolithography and electron-beam evaporation. The inner diameter of the ring patterned on the Ga_2O_3 layer measures $500 \mu\text{m}$, with a separation of $20 \mu\text{m}$ from the outer ring on the AlGaN:Si layer. After the lift-off step, the completed devices were subjected to a rapid annealing process at 850°C for 30 s in a N_2 environment to establish an Ohmic contact.

Material characterization

The atomic structure and chemical states of $\text{Ga}_2\text{O}_3/\text{AlN}$ (II)/N-polar AlGaN:Si film stack was analyzed using spherical aberration-corrected transmission electron microscopy (AC-TEM, FEI Tecnai F20) and X-ray photoelectron spectroscopy (XPS, VG ESCALAB LKII). Particularly, X-ray diffraction (XRD, Rigaku D/max-2500), atomic force microscopy (AFM, Bruker) and absorption spectra (Shimadzu UV-2600 spectrometer) were employed to assess the crystal quality, surface morphology and optical properties of the Ga_2O_3 and N-polar AlGaN:Si films.

Photoresponse measurements

For the as-formed devices, noise spectral density characteristics were measured with the FS380 Pro system (Platform Design Automation, Inc.), achieving a noise floor of $-10^{-28} \text{ A}^2 \text{ Hz}^{-1}$. Capacitance versus voltage (C - V) measurements were conducted using a semiconductor analyzer (B1500A) across a frequency range of 1 to 100 kHz. For evaluating the photoelectronic performance of the device, a testing setup consisting of a Xe lamp, a monochromator, and a Keithley 4200 parameter analyzer was utilized. The light intensity was regulated with a continuously variable attenuator and calibrated using a power meter (THORLABS, PM100USB). To evaluate the dynamic response of self-powered solar-blind photodetector, a pulse width of 25 ns and a frequency of 5 Hz, along with a spot size of 2 mm in diameter, was used as the optical input stimulus. The generated photocurrent pulses from the solar-blind photodetector were converted into pulsed voltage signals through a transimpedance amplifier and displayed on a connected oscilloscope (KEYSIGHT DSOS404A). The optical communication photoelectric waveform was tested with an MStarter 200 high precision photocurrent scanning test microscope (Nanjing METATEST Photoelectric Technology Co. Ltd). All experiments were conducted under ambient conditions at room temperature.

Theoretical calculations

All DFT calculations were performed by using the Vienna Ab Initio Simulation Package (VASP) along with the projector augmented wave method. And we employed the generalized gradient approximation of the Perdew–Burke–Ermerhof (PBE) method to consider the exchange correlation effect. The Grimme's D3 methods were applied to include vdW corrections for all DFT calculations. The cut-off energy, the energy convergence and force convergence criterion were 500 eV, 10^{-6} eV, and $0.01 \text{ eV } \text{\AA}^{-1}$, respectively. We adopted the spacing of reciprocal space sampling of 0.25 \AA^{-1} with a Gamma scheme to optimize all structures and calculated the relevant property. The DOS and charge

density difference results were analysed by the VASPKIT package. By evaluating the relative positions of the DOS peaks for the two components, we determined that the valence band maximum offset between AlN/Ga₂O₃ and AlGa_N:Si/AlN systems. Specially, to prevent the bandgap underestimation and obtain accurate band arrangement, we utilized the HSE06 hybrid functional to calculate the band structure of Ga₂O₃, AlN and AlGa_N:Si. The charge density difference was defined as: $\Delta\rho = \rho_{A/B} - \rho_A - \rho_B$, where $\rho_{A/B}$, ρ_A , and ρ_B represent the charge densities of the AlN/Ga₂O₃ (or AlGa_N:Si/AlN) heterojunction, isolated AlN, and isolated Ga₂O₃ (or AlGa_N:Si), respectively. To facilitate a comparative assessment of charge transfer strength between the two systems, we normalized the charge density difference to the cross-sectional area of each system (34 Å² for AlGa_N:Si/AlN and 58 Å² for AlN/Ga₂O₃). All the crystal structures are visualized by using VESTA.

Energy band structure simulation

The band structure and electric field distribution of the Ga₂O₃/AlN/AlGa_N:Si heterojunction were simulated by Silvaco TACD simulation, and numerical simulation was carried out in the software. Shockley-Read-Hall, Fermi-Dirac, and spontaneous polarization models were utilized to calculate the electric field distribution, energy band structure.

Solar-blind single-pixel imaging

The solar-blind single-pixel imaging experimental setup is equipped with a DMD, an imaging lens, a collection lens, and a single-pixel detector. The DMD, a pivotal component for pixel-wise modulation, consists of 1024 × 768 micro mirrors, each capable of toggling between two orientations at ±12° to represent binary states (1 and 0). The imaging subject is a circular mask model with a diameter of 11.9 mm, whose position is precision-controlled by a stepper motor. When illuminated by solar-blind light, the DMD modulates the speckle light field, which is then focused onto the object by the imaging lens. A solar-blind photodetector is positioned in the DMD's reflection path to capture the total echo signal for measurement.

Data availability

The source data generated in this study have been deposited in the figshare database under accession code <https://doi.org/10.6084/m9.figshare.29569640>. Additionally, all data are available from the corresponding authors upon request.

References

- Xie, C. et al. Recent progress in solar-blind deep-ultraviolet photodetectors based on inorganic ultrawide bandgap semiconductors. *Adv. Funct. Mater.* **29**, 1806006 (2019).
- Li, Z., Yan, T. & Fang, X. Low-dimensional wide-bandgap semiconductors for UV photodetectors. *Nat. Rev. Mater.* **8**, 587–603 (2023).
- Xu, M. S. et al. Electric-dipole gated two terminal phototransistor for charge-coupled device. *Adv. Opt. Mater.* **11**, 2300910 (2023).
- Yuan, Y. G. et al. Development of solar-blind AlGa_N 128 × 128 ultraviolet focal plane arrays. *Sci. China Ser. E Technol. Sci.* **51**, 820–826 (2008).
- Zheng, W., Jia, L. M. & Huang, F. Vacuum-ultraviolet photon detections. *iScience* **23**, 101145 (2020).
- McClintock, R. et al. 320×256 solar-blind focal plane arrays based on Al_xGa_{1-x}N. *Appl. Phys. Lett.* **86**, 011117 (2005).
- Qin, Y. et al. Ultra-high performance amorphous Ga₂O₃ photodetector arrays for solar-blind imaging. *Adv. Sci.* **8**, 2101106 (2021).
- Cai, Q. et al. Progress on AlGa_N-based solar-blind ultraviolet photodetectors and focal plane arrays. *Light Sci. Appl.* **94**, 10 (2021).
- Chen, Y. C. et al. Self-powered diamond/β-Ga₂O₃ photodetectors for solar-blind imaging. *J. Mater. Chem. C.* **21**, 5727–5732 (2018).
- Hou, X. H. et al. High-performance harsh-environment-resistant GaO_x solar-blind photodetectors via defect and doping engineering. *Adv. Mater.* **34**, 2106923 (2022).
- Qin, Y. et al. Amorphous gallium oxide-based gate-tunable high-performance thin film phototransistor for solar-blind imaging. *Adv. Electron. Mater.* **5**, 1900389 (2019).
- Chen, Y. C. et al. High-sensitive and fast MXene/silicon photodetector for single-pixel X-ray imaging. *InfoMat* **6**, 12596 (2024).
- Sun, M. J. et al. Single-pixel three-dimensional imaging with time-based depth resolution. *Nat. Commun.* **7**, 12010 (2016).
- Meng, H. Y. et al. Quantum dot-enabled infrared hyperspectral imaging with single-pixel detection. *Light Sci. Appl.* **13**, 121 (2024).
- Chen, X. H. et al. Review of gallium-oxide-based solar-blind ultraviolet photodetectors. *Photon. Res.* **7**, 381–415 (2019).
- Wu, C. et al. Review of self-powered solar-blind photodetectors based on Ga₂O₃. *Mater. Today Phys.* **28**, 100883 (2022).
- Chen, Y. F. et al. Unipolar barrier photodetectors based on van der Waals heterostructures. *Nat. Electron.* **4**, 357–363 (2021).
- Zhang, Q. Y. et al. Enhanced gain and detectivity of unipolar barrier solar blind avalanche photodetector via lattice and band engineering. *Nat. Commun.* **14**, 418 (2023).
- Jagtap, A. mardeep et al. Design of a unipolar barrier for a nanocrystal-based short-wave infrared photodiode. *ACS Photonics* **5**, 4569–4576 (2018).
- Ambacher, O. et al. Two-dimensional electron gases induced by spontaneous and piezoelectric polarization charges in N-and Ga-face AlGa_N/Ga_N heterostructures. *J. Appl. Phys.* **85**, 3222–3233 (1999).
- Brende, M. oritz et al. Measurement and simulation of top-and bottom-illuminated solar-blind AlGa_N metal-semiconductor-metal photodetectors with high external quantum efficiencies. *J. Appl. Phys.* **118**, 244504 (2015).
- Li, D. B. et al. AlGa_N photonics: recent advances in materials and ultraviolet devices. *Adv. Opt. Photon.* **10**, 43–110 (2018).
- Deurzen et al. Using both faces of polar semiconductor wafers for functional devices. *Nature* **634**, 334–340 (2024).
- Chaudhuri, R. eet et al. A polarization-induced 2D hole gas in undoped Gallium Nitride quantum wells. *Science* **365**, 1454–1457 (2019).
- Mita, S., Collazo, R. & Sitar, Z. Fabrication of a Ga_N lateral polarity junction by metalorganic chemical vapor deposition. *J. Cryst. Growth* **311**, 3044–3048 (2009).
- Guo, W. et al. Polarity control and fabrication of lateral polarity structures of III-nitride thin films and devices: progress and prospects. *J. Phys. D Appl. Phys.* **53**, 483002 (2020).
- Omori, T. et al. Reduction of dislocation density in lattice-relaxed Al_{0.68}Ga_{0.32}N film grown on periodical 1 μm spacing AlN pillar concave-convex patterns and its effect on the performance of UV-B laser diodes. *Appl. Phys. Express* **15**, 031004 (2022).
- Shimokawa, M. et al. Reduction of dislocation density in Al_{0.6}Ga_{0.4}N film grown on sapphire substrates using annealed sputtered AlN templates and its effect on UV-B laser diodes. *J. Cryst. Growth* **575**, 126325 (2021).
- Tao, H. C. et al. Improved crystal quality of AlGa_N by Al ion-implantation sapphire substrate. *Mater. Lett.* **351**, 135097 (2023).
- Zhou, X. et al. Tunneling diode based on WSe₂/SnS₂ heterostructure incorporating high detectivity and responsivity. *Adv. Mater.* **30**, 1703286 (2018).
- Tan, C. Y. et al. Broken-gap PtS₂/WSe₂ van der Waals heterojunction with ultrahigh reverse rectification and fast photoresponse. *ACS Nano* **15**, 8328–8337 (2018).
- Quoc, A. V. et al. Tuning carrier tunneling in van der Waals heterostructures for ultrahigh detectivity. *Nano Lett.* **17**, 453–459 (2017).

33. Chen, Y. et al. Ultra-sensitive flexible Ga₂O₃ solar-blind photo-detector array realized via ultra-thin absorbing medium. *Nano Res.* **15**, 3711–3719 (2022).
34. Wang, H. B. et al. Solar-blind UV photodetector with low-dark current and high-gain based on ZnO/Au/Ga₂O₃ sandwich structure. *Mater. Today Phys.* **24**, 100673 (2022).
35. Wang, Y. H. et al. Improved response speed of β-Ga₂O₃ solar-blind photodetectors by optimizing illumination and bias. *Mater. Des.* **221**, 110917 (2022).
36. Guo, D. Y. et al. Fabrication of β-Ga₂O₃/ZnO heterojunction for solar-blind deep ultraviolet photodetection. *Semicond. Sci. Technol.* **32**, 03LT01 (2017).
37. Wu, J. Q. When group-III nitrides go infrared: New properties and perspectives. *J. Appl. Phys.* **106**, 011101 (2019).
38. Gordon, L. et al. Hybrid functional calculations of DX centers in AlN and GaN. *Phys. Rev. B* **89**, 085204 (2014).
39. Chen, L. et al. Band-edge exciton states in AlN single crystals and epitaxial layers. *Appl. Phys. Lett.* **85**, 4334–4336 (2004).
40. Cao, J. Y. et al. Bidimensional carrier modulation in nanocolumn-array AlGaIn p-i-n ultraviolet photodiodes: achieving external quantum efficiency over 1000%. *Laser Photonics Rev.* 2500347 <https://doi.org/10.1002/lpor.202500347> (2025).
41. Zhang, H. C. et al. Superior AlGaIn/GaN-based phototransistors and Arrays with reconfigurable triple-mode functionalities enabled by voltage-programmed two-dimensional electron gas for high-quality Imaging. *Adv. Mater.* **36**, 2405874 (2024).
42. Guo, L. et al. Multiple-quantum-well-induced unipolar carrier transport multiplication in AlGaIn solar-blind ultraviolet photodiode. *Photonics Res.* **9**, 1907–1915 (2021).
43. Chen, Y. et al. Ferroelectric-tuned van der Waals heterojunction with band alignment evolution. *Nat. Commun.* **12**, 4030 (2021).
44. Jiang, H. Y. et al. Enhanced broadband photosensing and wavelength-resolved imaging via the piezo-pyroelectric effect in flexible CdS/pyramid-Si heterojunction. *Nano Energy* **137**, 110818 (2025).
45. Liu, J. H. et al. A new strategy of coupling pyroelectric and piezoelectric effects for photoresponse enhancement of a Cu(In,Ga)Se₂ heterojunction photodetector. *Adv. Funct. Mater.* **32**, 2208658 (2022).

Acknowledgements

This work was supported by the NSFC for Distinguished Young Scholars (No. 52025022), the National Key Research and Development Program of China (2021YFA0716404), the National Natural Science Foundation of China (No. 12474164, No. 62404038, No. 62301140, No. 52302166), the Postdoctoral Fellowship Program of CPSF (GZC20240240), the Science Technology Program of Jilin Province (NO. YDZJ202502CXJD081), the Research Projects of the Education Office of Jilin Province (JJKH20250300KJ), the Fundamental Research Funds for the Central Universities (No. 2412024QD009, No. 2412024QD005, No. 2412023QD004).

Author contributions

P.L., J.G.M., and H.B.W. conceived the project, designed the experiments, and coordinated the research. P.L., R.A., and H.M. performed the

heterostructure growth, including sputtering and MOCVD processes, and analyzed the film quality. H.B.W. fabricated the devices, conducted photolithography, etching, and electrode deposition, and contributed to electrical characterization. H.B.W. and P.L. carried out atomic-scale structural analysis using AC-TEM and XPS. C.Z. and H.B.W. designed and executed photoresponse measurements, dynamic testing and solar-blind single-pixel imaging experiments. L.Y., H.B.W., and P.L. supervised the theoretical calculations, including DFT simulations and energy band modeling using Silvaco TCAD, and interpreted the electronic structure data. H.B.W. and P.L. wrote the manuscript. J.G.M., H.Y.X., Y.C.L., R.A., and H.M. participated in the revision of the manuscript. All authors approved the final version. P.L. and J.G.M. oversaw the entire project and finalized the manuscript.

Competing interests

The authors declare no competing interests.

Additional information

Supplementary information The online version contains supplementary material available at <https://doi.org/10.1038/s41467-025-63683-w>.

Correspondence and requests for materials should be addressed to Peng Li, Jiangang Ma or Haiyang Xu.

Peer review information *Nature Communications* thanks Xiaosheng Fang and the other anonymous reviewer(s) for their contribution to the peer review of this work. A peer review file is available.

Reprints and permissions information is available at <http://www.nature.com/reprints>

Publisher's note Springer Nature remains neutral with regard to jurisdictional claims in published maps and institutional affiliations.

Open Access This article is licensed under a Creative Commons Attribution-NonCommercial-NoDerivatives 4.0 International License, which permits any non-commercial use, sharing, distribution and reproduction in any medium or format, as long as you give appropriate credit to the original author(s) and the source, provide a link to the Creative Commons licence, and indicate if you modified the licensed material. You do not have permission under this licence to share adapted material derived from this article or parts of it. The images or other third party material in this article are included in the article's Creative Commons licence, unless indicated otherwise in a credit line to the material. If material is not included in the article's Creative Commons licence and your intended use is not permitted by statutory regulation or exceeds the permitted use, you will need to obtain permission directly from the copyright holder. To view a copy of this licence, visit <http://creativecommons.org/licenses/by-nc-nd/4.0/>.

© The Author(s) 2025